nanomaterials

MDPI

Article

MOF-Derived $CoSe_2$@NiFeOOH Arrays for Efficient Oxygen Evolution Reaction

Yulong Tang [1,2,†], Jiangning Li [1,2,†], Zhiyi Lu [2,3], Yunan Wang [2,3,*], Kai Tao [1,*] and Yichao Lin [2,3,*]

[1] School of Materials Science & Chemical Engineering, Ningbo University, Ningbo 315211, China; tangyulong@nimte.ac.cn (Y.T.); lijiangning@nimte.ac.cn (J.L.)
[2] Key Laboratory of Advanced Fuel Cells and Electrolyzers Technology of Zhejiang Province, Ningbo Institute of Materials Technology and Engineering, Chinese Academy of Sciences, Ningbo 315201, China; luzhiyi@nimte.ac.cn
[3] University of Chinese Academy of Sciences, Beijing 100049, China
* Correspondence: wangyunan@nimte.ac.cn (Y.W.); taokai@nbu.edu.cn (K.T.); yclin@nimte.ac.cn (Y.L.)
† These authors contributed equally to this work.

Abstract: Water electrolysis is a compelling method for the production of environmentally friendly hydrogen, minimizing carbon emissions. The electrolysis of water heavily relies on an effective and steady oxygen evolution reaction (OER) taking place at the anode. Herein, we introduce a highly promising catalyst for OER called $CoSe_2$@NiFeOOH arrays, which are supported on nickel foam. This catalyst, referred to as $CoSe_2$@NiFeOOH/NF, is fabricated through a two-step process involving the selenidation of a Co-based porous metal organic framework and subsequent electrochemical deposition on nickel foam. The $CoSe_2$@NiFeOOH/NF catalyst demonstrates outstanding activity for the OER in an alkaline electrolyte. It exhibits a low overpotential (η) of 254 mV at 100 mA cm^{-2}, a small Tafel slope of 73 mV dec^{-1}, and excellent high stability. The good performance of $CoSe_2$@NiFeOOH/NF can be attributed to the combination of the high conductivity of the inner layer and the synergistic effect between $CoSe_2$ and NiFeOOH. This study offers an effective method for the fabrication of highly efficient catalysts for an OER.

Keywords: oxygen evolution reaction; NiFeOOH; water electrolysis; selenidation; $CoSe_2$

Citation: Tang, Y.; Li, J.; Lu, Z.; Wang, Y.; Tao, K.; Lin, Y. MOF-Derived $CoSe_2$@NiFeOOH Arrays for Efficient Oxygen Evolution Reaction. *Nanomaterials* **2023**, *13*, 2621. https://doi.org/10.3390/nano13192621

Academic Editor: Jooheon Kim

Received: 28 August 2023
Revised: 16 September 2023
Accepted: 19 September 2023
Published: 22 September 2023

1. Introduction

The storage of renewable energy presents a significant challenge to constructing an environmentally friendly energy system [1–6]. Water electrolysis has become a promising technology for storing electricity generated from renewable sources by converting it into a clean energy carrier, H_2. It involves two distinct half-reactions: an hydrogen evolution reaction (HER) occurring at the cathode and an oxygen evolution reaction (OER) taking place at the anode [7–10]. Relative to the HER, the OER suffers from much more sluggish kinetics, and so, it requires highly efficient electrocatalysts. Thus far, Ir- and Ru-based materials represent state-of-the-art OER electrocatalysts because of their high activity level and stability [11–17]. However, the high cost and scarcity of these resources limit their extensive utilization [12,18–20]. Therefore, it is crucial to develop alternative, affordable electrocatalysts that are abundant in the Earth's crust. Transition metal chalcogenides (TMCs) with the formula M_xC_y (M = Fe, Co, and Ni; C = S and Se) have gained significant interest for their good performance in OER catalysis, as well as their low cost and abundance in the Earth's crust [21]. Yang Shao-Horn and colleagues conducted the catalytic analysis of perovskite oxide, where they elucidated a correlation between OER activity and the occupancy of 3D electrons with e_g symmetry in transition metal cations on the surface. Their findings revealed that an optimized OER electrocatalyst possesses e_g occupancy of approximate one [22]. Liu et al. applied this principle to explain the high OER activity of $CoSe_2$, which exhibits a $t_{2g}6e_g1$ electronic configuration, approaching the optimal e_g

filling [23,24]. However, they overlooked the surface reconstruction or oxidation of $CoSe_2$ under OER catalysis. The surface reconstruction of catalysts was frequently observed in the OER test. For example, Shahid et al. synthesized a catalyst for the OER, which consists of cobalt-containing ester salts of polyoxometalates that are immobilized on carbon nanotube fibers (Co_4POM@CNTF). The catalyst showcases an exceptional OER performance and remarkable stability in alkaline solutions, which can be attributed to the efficient transfer of electrons and the enhanced electrochemical active surface area of the self-activating electrocatalyst that is affixed to the highly conductive carbon nanotube fibers [25]. Theoretically, the surface oxidation of $CoSe_2$ would lead to the generation of Co oxides or hydroxides on the $CeSe_2$ surface. This indicates that the actual catalytic phase occurs with the Co oxides/hydroxides rather than $CoSe_2$. Therefore, the inner $CoSe_2$ serves as an electron-transfer conductor and is also probably influenced by the electronic structure of the surface Co oxides/hydroxides. Based on the above analysis, we are inclined to believe that the good OER catalytic performance of $CoSe_2$ may result from the synergistic effect of the surface oxides and the inner $CoSe_2$.

NiFe-layered double-hydroxide (NiFe-LDH) and NiFeOOH species have been recognized as very efficient OER electrocatalysts both in theoretical calculations and experimental investigations [26,27]. For example, Du and coworkers prepared an OER catalyst of NiO/NiFe-LDH, which demonstrated an OER overpotential of only 205 mV at a current density of 30 mA cm^{-2}, with a Tafel slope of merely 30 mV dec^{-1} in 1 M KOH solution [27].

This good catalytic performance is achieved by adjusting the adsorption energy of each intermediate, which effectively bypasses the scaling relationship. Hu et al. conducted a comprehensive investigation on FeOOH-NiOOH and NiFe LDH, unveiling the distinct electrochemical and spectroscopic characteristics between the two catalysts, despite their similar chemical compositions. Notably, in FeOOH-NiOOH, a significant portion of iron ions were observed to reside within surface γ-FeOOH clusters, contrasting the doping of iron ions within the lattice of $Ni(OH)_2$/NiOOH in NiFe LDH. This discrepancy played a crucial role in the remarkable tenfold enhancement of OER activity witnessed in FeOOH-NiOOH compared to that of NiFe LDH [26].

Based on the above, we proposed to fabricate thin NiFeOOH onto a $CoSe_2$ surface, aiming to achieve an optimized OER performance through the synergistic effect of NiFeOOH and $CoSe_2$. To increase the accessibility of $CoSe_2$, we prepared it via the selenidation of a Co-based metal–organic framework (MOF, ZIF-L) array grown on Ni foam [28–30]. ZIF-L is selected as the precursor because it has a thin leaf morphology and can be readily grown on nickel foam, which facilitate the following selenidation. The deposition of NiFeOOH onto $CoSe_2$ was achieved through electrochemical deposition (Figure 1). The $CoSe_2$@NiFeOOH/NF composite exhibited a good performance in alkaline electrolytes for the OER, demonstrating an overpotential of 254 mV at a current density of 100 mA cm^{-2} and a Tafel slope of 73 mV dec^{-1}. Furthermore, it showed excellent stability with negligible current density decay after 100 h of operation. The high OER activity level can be attributed to the increased exposure of active sites and the synergistic effect of NiFeOOH outer layer and $CoSe_2$ inner layer.

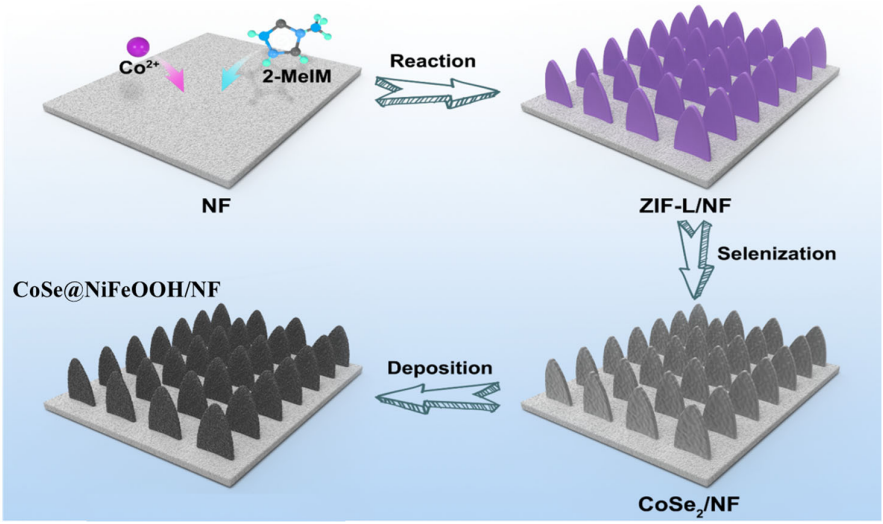

Figure 1. Schematic illustration of the routes to $CoSe_2$@NiFeOOH/NF.

2. Experimental Section

2.1. Materials

$Co(NO_3)_2 \cdot 6H_2O$, 2-methylimidazole (2-MeIM, 99%), $Ni(NO_3)_2 \cdot 6H_2O$, $Fe(NO_3)_3 \cdot 9H_2O$, sodium borohydride ($NaBH_4$), selenium powder (Se), and absolute ethanol were purchased from Aladdin. Ni was obtained from J&K Chemical Technology (San Jose, CA, USA) and subsequently subjected to sonication with acetone, ethanol, and deionized water for 30 min each prior to use.

2.2. Preparation of Cobalt-Based ZIF-L/NF

Initially, a solution of 2×10^{-3} mol Co $(NO_3)_2$ and another solution of 1.6×10^{-2} mol 2-MeIM were prepared by dissolving them individually in 40 mL of deionized water in a beaker. Then, the two solutions were combined via stirring. Subsequently, nickel foam (NF) measuring 2 × 3 cm was immersed in the mixture and left at room temperature for 4 h to generate ZIF-L/NF. To prepare it for future use, ZIF-L/NF was subjected to three rounds of rinsing with both ethanol and deionized water. Subsequently, it was dried overnight in an oven at 60 °C.

2.3. Synthesis of $CoSe_2$/NF

The ZIF-L/NF selenidation process was carried out using a hydrothermal method. Initially, 60 mg of $NaBH_4$ was completely dissolved in 25 mL of deionized water. Subsequently, 20 mg of selenium powder was added to the solution. The mixture was continuously stirred for 40 min until a light-yellow solution was formed. The solution was then transferred into a Teflon-lined stainless steel autoclave, and a ZIF-L/NF sample with dimensions of 1 cm × 1.5 cm was immersed in the solution. The autoclave was kept at a temperature of 180 °C for a duration of 8 h. Afterward, the resulting $CoSe_2$/NF product was rinsed with ethanol and water and finally dried in an oven at a temperature of 60 °C for 12 h.

2.4. Synthesis of $CoSe_2$@NiFeOOH/NF

The $CoSe_2$@NiFeOOH/NF composite was synthesized via electrochemical deposition with $CoSe_2$/NF as the working electrode in a solution containing $Ni(NO_3)_2$ and $Fe(NO_3)_3$ (molar ratio of Ni^{2+}/Fe^{3+} = 4:1). The electrochemical deposition was conducted at a constant potential of −1.4 V vs. RHE for 8 s.

2.5. Characterization

X-ray power diffraction (XRD) data were recorded on a Bruker D8 ADVANCE DAVINCI. The morphologies and nanostructures were probed using field emission scanning electron

microscopy (SEM, Hitachi S-4800, Japan) and transmission electron microscopy (TEM, Tecnai F20, JEM-ARM200F, USA). The surface chemical valences of the samples were analyzed using X-ray photoelectron spectroscopy (XPS) (Axis SUPRA Kratos, UK).

2.6. Electrocatalytic Measurement

The electrochemical measurements were conducted on a CHI760E electrochemical workstation. The as-prepared samples served as the working electrode (geometric area: 1.0 cm^2). The counter electrode was a Pt mesh with dimensions of 1 cm × 1 cm, and an Ag/AgCl electrode was used as the reference electrode. A 1.0 M KOH electrolyte was utilized. To convert the measured potentials to the reversible hydrogen electrode (RHE) scale, the following equation was used: $E_{RHE} = E_{Ag/AgCl} + 0.059\ pH + 0.197\ V$. Linear sweep voltammetry (LSV) curves were measured at a scan rate of 5 mV s^{-1}, while cyclic voltammetry (CV) curves were recorded at scan rates ranging from 10 to 50 mV s^{-1}. Electrochemical impedance spectra (EIS) were measured at 1.52 V vs. RHE. All the polarization curves were IR-corrected. The double-layer capacitances were determined by analyzing the CV curves obtained at different scan rates, ranging from 10 to 50 mV s^{-1}. The stability of the electrocatalyst was evaluated through chrono-amperometry performed at a constant potential. The Faraday efficiency (FE) was determined using the bubbling method following the formula: $FE = 4 \times F \times V/(1000 \times V_m \times It)$, where V is the rising volume (mL) of the soap bubble over time t, I is the current density (It representing the total number of charges transferred under constant current), V_m is the molar volume (24.5 L mol^{-1} at 25 °C), and F is the Faraday constant (96,485 C mol^{-1}).

3. Results and Discussion

ZIF-L was deposited onto NF prepared by facilely immersing NF into a solution of cobalt nitrate and 2-methylimidazole at room temperature. The morphology of the ZIF-L/NF sample was analyzed via SEM, which allows the detailed imaging of the sample surface at high magnification. The crystal structure of the synthesized catalyst was determined using powder XRD. Figure 2a,d,g illustrates the triangular ZIF-L plates with smooth surfaces vertically aligned on the NF. The sharp diffraction peaks at 44.5°, 51.9°, and 76.2° are attributed to the Ni substrate, and the peak at 29.4° belongs to ZIF-L. This confirms the successful fabrication of ZIF-L on NF. After selenization, ZIF-L transformed into the $CoSe_2$ phase while maintaining its morphology, except that the surface became rougher (Figure 2b,e,h). Subsequently, NiFeOOH was electrochemically deposited onto $CoSe_2$, resulting in a morphological change, where $CoSe_2$ formed an array with increased surface roughness and additional folds. The XRD analysis of the $CoSe_2$@NiFeOOH/NF sample showed no visible peaks except those of the Ni substrate, suggesting an amorphous structure in the NiFeOOH layer [31]. The absence of XRD signals for $CoSe_2$ demonstrates that a relatively compact NiFeOOH layer formed on the $CoSe_2$ surface. The three-dimensional $CoSe_2$@NiFeOOH can aid in the transportation of electrolytes and the diffusion of reactive gases, thereby accelerating the reaction process [31].

The detailed morphology of $CoSe_2$@NiFeOOH was further characterized via TEM. Figure 3a shows that $CoSe_2$@NiFeOOH possesses a thin-leaf-like morphology. The weak polycrystalline rings in the selected area electron diffraction (SAED) pattern (Figure 3c) indicate the poor crystallization of these thin leaf structures in the single derived $CoSe_2$@NiFeOOH sample. The structure of $CoSe_2$@NiFeOOH/NF was precisely characterized using high-resolution TEM (HRTEM). On the top surface of $CoSe_2$@NiFeOOH, two fringes with lattice spacings of 0.259 and 0.223 nm were observed, corresponding to the (111) and (210) planes of $CoSe_2$, respectively (Figure 3b). Elemental mapping images demonstrate the homogeneous dispersion of Ni, Fe, Co, Se, and O elements throughout the entire $CoSe_2$@NiFeOOH/NF, with an atomic ratio of Ni:Fe:Co:Se:O = 24:6:29:3:38 (Figure S2).

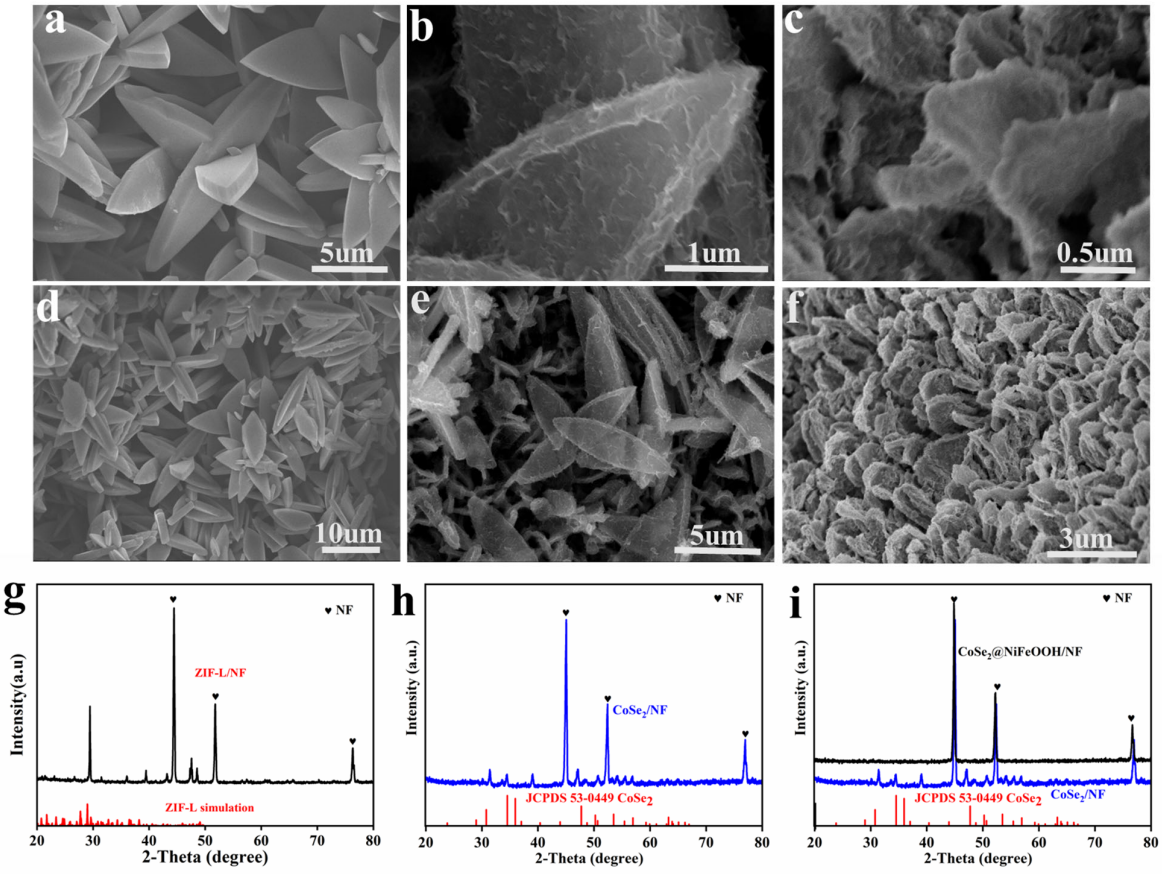

Figure 2. SEM images of (**a**,**d**) ZIF-L, (**b**,**e**) $CoSe_2$, and (**c**,**f**) $CoSe_2$@NiFeOOH/NF. XRD patterns of (**g**) ZIF-L/NF, (**h**) $CoSe_2$/NF, and (**i**) $CoSe_2$@NiFeOOH/NF.

X-ray photoelectron spectroscopy (XPS) measurements were taken to analyze the elemental composition and chemical valence states of the as-prepared $CoSe_2$@NiFeOOH/NF. As shown in Figure 4a, two peaks centered at 855.7 and 873.5 eV were identified as the main peaks corresponding to oxidized Ni $2p_{3/2}$ and Ni $2p_{1/2}$, respectively. Another two peaks at 861.2 and 879.3 eV were attributed to the shake-up satellite peak [32]. Figure 4b displays the Co $2p_{1/2}$ and Co $2p_{3/2}$ peaks, which can be further divided into four peaks located at 796.8/780.8 eV (Co^{2+}) and 783.8/802.2 eV (Co^{3+}). This suggests that the Co atom in $CoSe_2$@NiFeOOH/NF is predominantly in the valence states of +2 and +3 [33]. Due to the overlap of the 2p peak of Fe with the Auger peak of Co, it is impossible to deconvolute the Fe 2p XPS peak. Nevertheless, we can determine the presence of Fe and its oxidation state from the two peaks in the XPS raw data of Fe 2p. In the XPS spectra of Fe 2p (Figure 4c), two characteristic peaks at 711.1 and 724.6 eV correspond to Fe $2p_{3/2}$ and Fe $2p_{1/2}$, respectively, indicating the presence of Fe^{3+} [33]. The findings collectively indicate that Ni and Fe exist in Ni and Fe oxidation states in $CoSe_2$@NiFeOOH/NF. In addition, as shown in Figure 4d, Se $3d_{5/2}$ (54.7 eV) and Se $3d_{3/2}$ (55.4 eV) confirm the existence of selenium–metal bonds, while the peak at 59.2 eV corresponds to a Se-O bond, which is due to the surface oxidation in the air environment [34–37].

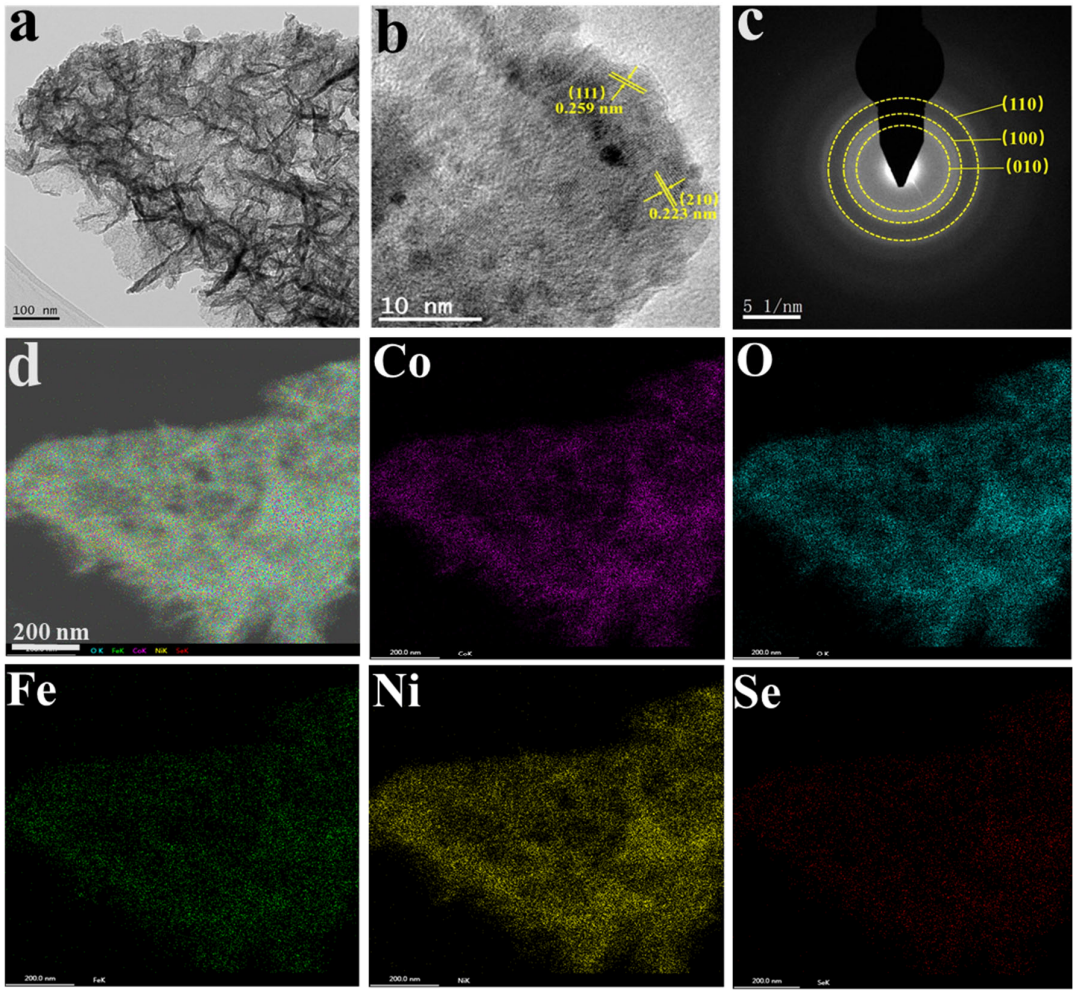

Figure 3. (**a**) TEM, (**b**) HRTEM, (**c**) SAED pattern, and (**d**) STEM images and the corresponding elemental mapping images of Co, O, Fe, Ni, and Se of $CoSe_2$@NiFeOOH/NF.

The catalysts' OER performance was assessed using an electrochemical three-electrode system in 1 M KOH alkaline solution. As shown in Figure 5a, $CoSe_2$@NiFeOOH/NF exhibits an overpotential of 254 mV at 100 mA cm^{-2}, which is significantly lower than those of $CoSe_2$/NF, NiFe-LDH/NF, NF/Selenization, $CoSe_2$@NiOOH/NF, and $CoSe_2$@FeOOH/NF. The OER performance of $CoSe_2$@NiFeOOH/NF is comparable to those of other reported OER electrocatalysts, such as $NiSe_2$-$CoSe_2$ [38], SiO_2/Co_xP [39], and $Ni(OH)_2$@NiS_2 [40] (Table S1). The Tafel slopes of the four samples, namely $CoSe_2$@FeOOH/NF, $CoSe_2$@NiOOH/NF, $CoSe_2$/NF, and $CoSe_2$@NiFeOOH/NF, were calculated to analyze their kinetics. As shown in Figure 5c, $CoSe_2$@NiFeOOH possesses the smallest Tafel slope of 73 mV dec^{-1}, which is much smaller than those of $CoSe_2$@FeOOH/NF (102 mV dec^{-1}), $CoSe_2$/NF (119 mV dec^{-1}), and $CoSe_2$@NiOOH/NF (126 mV dec^{-1}), suggesting faster OER kinetics. To gain further insight into the kinetics of electron transfer, EIS measurements were taken. Figure 5b displays the Nyquist plots of all the samples. Notably, the $CoSe_2$@NiFeOOH/NF sample exhibits the smallest diameter of the semicircle in the high frequency region, which unequivocally confirms the presence of charge transfer resistance (R_{ct}). This resistance facilitates smooth charge transfer, ultimately resulting in excellent oxygen evolution reaction (OER) activity. Additionally, to understand the intrinsic catalytic activity of $CoSe_2$@NiFeOOH/NF for the OER, the electrochemical surface area (ECSA) was estimated by measuring the double-layer capacitance (C_{dl}) in the potential range of 1.07–1.17 V at scan rates ranging from 10 to 50 mV s^{-1} (Figure S1). Interestingly, $CoSe_2$@NiFeOOH/NF exhibits the highest Cdl value of 29.0 mF cm^{-2} among all the samples, surpassing those

of $CoSe_2$@NiOOH/NF (23.1 mF cm^{-2}) and $CoSe_2$@FeOOH/NF (20.5 mF cm^{-2}). Furthermore, the electrocatalytic stability of $CoSe_2$@NiFeOOH/NF was evaluated. As depicted in Figure 5h, the current variation is negligible after a 100 h continuous test at 1.54 V. Furthermore, we also probed the morphology and electronic structural characterization of $CoSe_2$@NiFeOOH/NF after a 100 h stability test. As shown in Figures S3 and S4, no visible variation in the XPS spectra and morphology of $CoSe_2$@NiFeOOH/NF after the stability test was observed, demonstrating excellent stability.

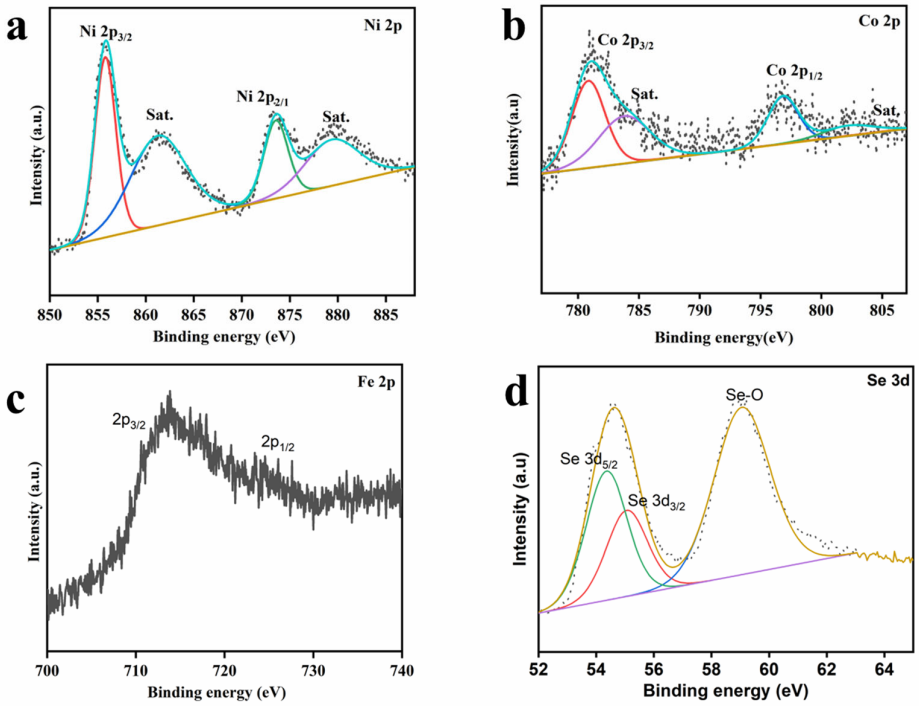

Figure 4. High-resolution XPS spectra of $CoSe_2$@NiFeOOH/NF (**a**) Ni, (**b**) Co, (**c**) Fe, (**d**) Se.

The overpotential increase for every 50 mA cm^{-2} of current density is illustrated in Figure 5f. It is evident from Figure 5a that $CoSe_2$@NiFeOOH/NF has a significantly lower overpotential than those of $CoSe_2$@FeOOH/NF and $CoSe_2$@NiOOH/NF, signifying the higher catalytic activity level of $CoSe_2$@NiFeOOH. Figure 5e illustrates the chronopotentiometric curve of $CoSe_2$@NiFeOOH, showing multiple steps with the current density incrementing from 10 to 100 mA cm^{-2} in ten steps. In the initial step, the potential rapidly stabilizes at 1.44 V and remains nearly constant for a duration of 320 s. Similar phenomena are observed in subsequent steps, indicating the exceptional mass transport and electronic conductivity characteristics of $CoSe_2$@NiFeOOH/NF. The Faradaic efficiency of the OER with the $CoSe_2$@NiFeOOH/NF electrodes was evaluated by measuring the O_2 produced during a constant current test experiment. According to Figure 5g, the measured amount of O_2 is in close agreement with the theoretical yield, resulting in a remarkable Faradaic efficiency of 97.8% for the $CoSe_2$@NiFeOOH/NF electrode.

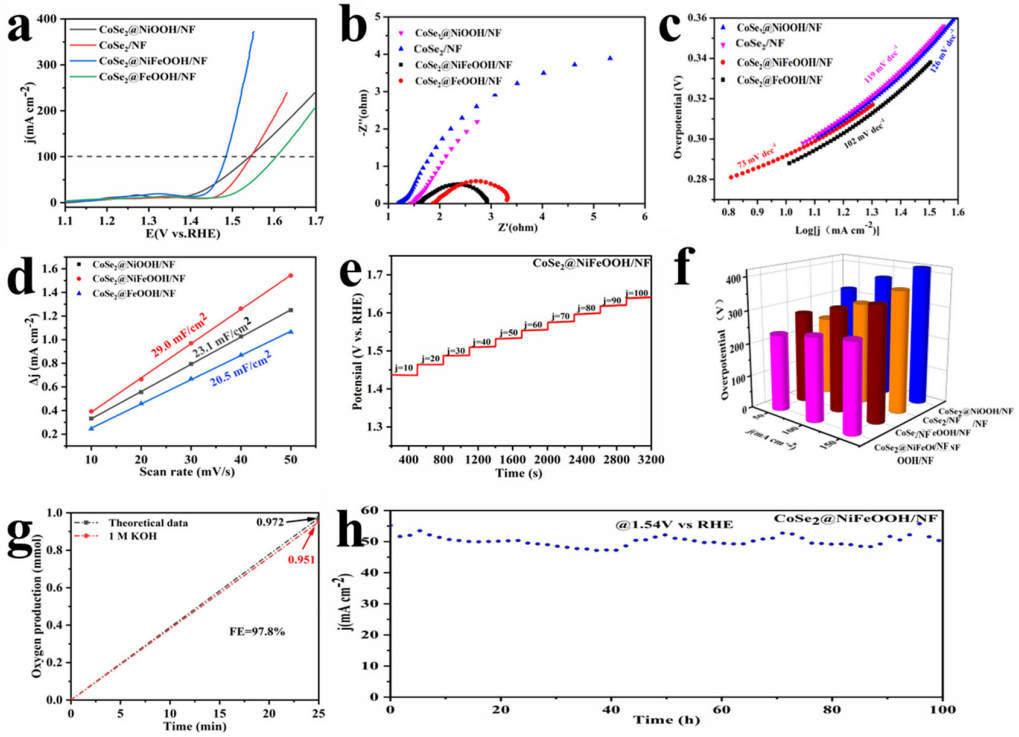

Figure 5. (**a**) LSV curves for $CoSe_2$/NF, $CoSe_2$@FeOOH/NF, $CoSe_2$@NiOOH/NF, NiFe-LDH/NF, NF/selenization, and $CoSe_2$@NiFeOOH/NF. (**b**) EIS curves, (**c**) Tafel plots, and (**d**) C_{dl} plots. (**e**) Rate capability evaluation of $CoSe_2$@NiFeOOH/NF. (**f**) Catalyst overpotentials at different current densities. (**g**) Faraday efficiency. (**h**) i–t curve for $CoSe_2$@NiFeOOH at the η = 0.31 V for 100 h.

4. Conclusions

In summary, a three-dimensional $CoSe_2$@NiFeOOH sample supported on nickel foam for efficient OER catalysis was fabricated. The excellent conductivity of $CoSe_2$ and the synergistic effect between $CoSe_2$ and NiFeOOH facilitate OER catalysis on $CoSe_2$@NiFeOOH/NF. The $CoSe_2$@NiFeOOH/NF catalyst demonstrated an excellent performance in the alkaline electrolyte, achieving an overpotential of 254 mV at 100 mA cm^{-2} and a Tafel slope of 73 mV dec^{-1}. Furthermore, the catalyst demonstrated remarkable stability with minimal decay in the current density, even after 100 h. The findings of this study represent a prototype of a synergistic strategy for creating highly efficient electrocatalysts.

Supplementary Materials: The following supporting information can be downloaded at: https://www.mdpi.com/article/10.3390/nano13192621/s1. Figure S1. CV curves of (a) CoSe2@FeOOH/NF. (b) CoSe2@NiFeOOH/NF and c) $CoSe_2$@NiOOH/NF. Figure S2. Elemental mapping images of Co, O, Fe, Ni, and Se. Figure S3. (a) TEM, (b) HRTEM, (c) SAED pattern, and (d) STEM images and the corresponding elemental mapping images of Co, O, Fe, Ni, and Se of $CoSe_2$@NiFeOOH/NF after 100 h durability test. Figure S4. High-resolution XPS spectra of $CoSe_2$@NiFeOOH/NF after 100 h durability test. Table S1. Comparison of the OER activity of $CoSe_2$@NiFeOOH/NF with other non-noble metal electrocatalysts in alkaline solution. References [41–52] are cited in the Supplementary Materials.

Author Contributions: Conceptualization, Y.L., Y.W. and K.T.; methodology, Y.L., Y.T., Z.L. and J.L.; formal analysis, J.L., Y.T., Y.W. and Y.L.; investigation, Y.T. and J.L.; data curation, Y.T. and J.L.; writing—original draft preparation Y.T. and J.L.; writing—review and editing, Y.L. and Y.W.; supervision, Y.L. and K.T.; project administration, Y.L., Y.T. and J.L.; funding acquisition, Y.L. and Y.W. All authors have read and agreed to the published version of the manuscript.

Funding: This research was funded by R&D Program of Zhejiang (No. 2022C01029), National Natural Science Foundation of China (No. 52271232), Bellwethers Project of Zhejiang Research and Development Plan (2022C01158), Natural Science Foundation of Zhejiang Province (No. LY21E020008), Youth

Innovation Promotion Association, CAS (No. 2020300), Ningbo S&T Innovation 2025 Major Special Program (2022Z205), and Jiangbei Science and Technology planning project (202301A09).

Data Availability Statement: We would like to share our data upon request from the authors.

Conflicts of Interest: The authors declare no conflict of interest.

References

1. Dresp, S.; Ngo Thanh, T.; Klingenhof, M.; Brückner, S.; Hauke, P.; Strasser, P. Efficient direct seawater electrolysers using selective alkaline NiFe-LDH as OER catalyst in asymmetric electrolyte feeds. *Energy Environ. Sci.* **2020**, *13*, 1725–1729. [CrossRef]
2. Wang, Y.; Tao, S.; Lin, H.; Wang, G.; Zhao, K.; Cai, R.; Tao, K.; Zhang, C.; Sun, M.; Hu, J.; et al. Atomically targeting NiFe LDH to create multivacancies for OER catalysis with a small organic anchor. *Nano Energy* **2021**, *81*, 105606. [CrossRef]
3. Sun, H.; Zhang, W.; Li, J.-G.; Li, Z.; Ao, X.; Xue, K.-H.; Ostrikov, K.K.; Tang, J.; Wang, C. Rh-engineered ultrathin NiFe-LDH nanosheets enable highly-efficient overall water splitting and urea electrolysis. *Appl. Catal. B Environ.* **2021**, *284*, 119740. [CrossRef]
4. Alobaid, A.; Wang, C.; Adomaitis, R.A. Mechanism and kinetics of HER and OER on NiFe LDH films in an alkaline electrolyte. *J. Electrochem. Soc.* **2018**, *165*, J3395–J3404. [CrossRef]
5. Hunter, B.M.; Hieringer, W.; Winkler, J.R.; Gray, H.B.; Müller, A.M. Effect of interlayer anions on NiFe-LDH nanosheet water oxidation activity. *Energy Environ. Sci.* **2016**, *9*, 1734–1743. [CrossRef]
6. Wang, Y.; Yan, D.; El Hankari, S.; Zou, Y.; Wang, S. Recent progress on layered double hydroxides and their derivatives for electrocatalytic water splitting. *Adv. Sci.* **2018**, *5*, 1800064. [CrossRef]
7. Tang, Y.; Liu, Q.; Dong, L.; Wu, H.B.; Yu, X.-Y. Activating the hydrogen evolution and overall water splitting performance of NiFe LDH by cation doping and plasma reduction. *Appl. Catal. B Environ.* **2020**, *266*, 118627. [CrossRef]
8. Hu, L.; Zeng, X.; Wei, X.; Wang, H.; Wu, Y.; Gu, W.; Shi, L.; Zhu, C. Interface engineering for enhancing electrocatalytic oxygen evolution of NiFe LDH/NiTe heterostructures. *Appl. Catal. B Environ.* **2020**, *273*, 119014. [CrossRef]
9. Nayak, S.; Parida, K. Superactive NiFe-LDH/graphene nanocomposites as competent catalysts for water splitting reactions. *Inorg. Chem. Front.* **2020**, *7*, 3805–3836. [CrossRef]
10. Yu, J.; Yu, F.; Yuen, M.-F.; Wang, C. Two-dimensional layered double hydroxides as a platform for electrocatalytic oxygen evolution. *J. Mater. Chem. A* **2021**, *9*, 9389–9430. [CrossRef]
11. Chen, S.; Huang, H.; Jiang, P.; Yang, K.; Diao, J.; Gong, S.; Liu, S.; Huang, M.; Wang, H.; Chen, Q. Mn-doped RuO2 nanocrystals as highly active electrocatalysts for enhanced oxygen evolution in acidic media. *ACS Catal.* **2019**, *10*, 1152–1160. [CrossRef]
12. Hubert, M.A.; Patel, A.M.; Gallo, A.; Liu, Y.; Valle, E.; Ben-Naim, M.; Sanchez, J.; Sokaras, D.; Sinclair, R.; Nørskov, J.K.; et al. Acidic oxygen evolution reaction activity–stability relationships in Ru-based pyrochlores. *ACS Catal.* **2020**, *10*, 12182–12196. [CrossRef]
13. Liao, J.; Zaman, S.; Wang, Y.; Yang, M.; Yang, L.; Chen, M.; Wang, H. Improved reversal tolerant properties of IrO(x) as an anode electrocatalyst in proton exchange membrane fuel cells. *ACS Appl. Mater. Interfaces* **2023**, *15*, 4092–4100. [CrossRef] [PubMed]
14. Jin, H.; Choi, S.; Bang, G.J.; Kwon, T.; Kim, H.S.; Lee, S.J.; Hong, Y.; Lee, D.W.; Park, H.S.; Baik, H.; et al. Safeguarding the RuO_2 phase against lattice oxygen oxidation during acidic water electrooxidation. *Energy Environ. Sci.* **2022**, *15*, 1119–1130. [CrossRef]
15. Lin, Y.; Tian, Z.; Zhang, L.; Ma, J.; Jiang, Z.; Deibert, B.J.; Ge, R.; Chen, L. Chromium-ruthenium oxide solid solution electrocatalyst for highly efficient oxygen evolution reaction in acidic media. *Nat. Commun.* **2019**, *10*, 162–175. [CrossRef] [PubMed]
16. Retuerto, M.; Pascual, L.; Calle-Vallejo, F.; Ferrer, P.; Gianolio, D.; Pereira, A.G.; Garcia, A.; Torrero, J.; Fernandez-Diaz, M.T.; Bencok, P.; et al. Na-doped ruthenium perovskite electrocatalysts with improved oxygen evolution activity and durability in acidic media. *Nat. Commun.* **2019**, *10*, 2041–2050. [CrossRef]
17. Zaman, S.; Wang, M.; Liu, H.; Sun, F.; Yu, Y.; Shui, J.; Chen, M.; Wang, H. Carbon-based catalyst supports for oxygen reduction in proton-exchange membrane fuel cells. *Trends Chem.* **2022**, *4*, 886–906. [CrossRef]
18. An, L.; Wei, C.; Lu, M.; Liu, H.; Chen, Y.; Scherer, G.G.; Fisher, A.C.; Xi, P.; Xu, Z.J.; Yan, C.H. Recent development of oxygen evolution electrocatalysts in acidic environment. *Adv. Mater.* **2021**, *33*, e2006328. [CrossRef]
19. Li, L.; Wang, P.; Shao, Q.; Huang, X. Recent progress in advanced electrocatalyst design for acidic oxygen evolution reaction. *Adv. Mater.* **2021**, *33*, e2004243.
20. Spori, C.; Kwan, J.T.H.; Bonakdarpour, A.; Wilkinson, D.P.; Strasser, P. The stability challenges of oxygen evolving catalysts: Towards a common fundamental understanding and mitigation of catalyst degradation. *Angew. Chem. Int. Ed.* **2017**, *56*, 5994–6021.
21. Zhang, T.; Hang, L.; Sun, Y.; Men, D.; Li, X.; Wen, L.; Lyu, X.; Li, Y. Hierarchical hetero-Ni3Se4@NiFe LDH micro/nanosheets as efficient bifunctional electrocatalysts with superior stability for overall water splitting. *Nanoscale Horiz.* **2019**, *4*, 1132–1138. [CrossRef]
22. Suntivich, J.; May, K.J.; Gasteiger, H.A.; Goodenough, J.B.; Shao-Horn, Y. A perovskite oxide optimized for oxygen evolution catalysis from molecular orbital principles. *Science* **2011**, *334*, 1383–1385. [CrossRef]
23. Liu, Y.; Cheng, H.; Lyu, M.; Fan, S.; Liu, Q.; Zhang, W.; Zhi, Y.; Wang, C.; Xiao, C.; Wei, S.; et al. Low overpotential in vacancy-rich ultrathin $CoSe_2$ nanosheets for water oxidation. *J. Am. Chem. Soc.* **2014**, *136*, 15670–15675. [CrossRef]

24. Li, J.G.; Sun, H.; Lv, L.; Li, Z.; Ao, X.; Xu, C.; Li, Y.; Wang, C. Metal-organic framework-derived hierarchical (Co,Ni)Se_2@NiFe LDH hollow nanocages for enhanced oxygen evolution. *ACS Appl. Mater. Interfaces* **2019**, *11*, 8106–8114. [CrossRef] [PubMed]
25. Tariq, I.; Asghar, M.A.; Ali, A.; Badshah, A.; Abbas, S.M.; Iqbal, W.; Zubair, M.; Haider, A.; Zaman, S. Surface reconstruction of Cobalt-Based polyoxometalate and CNT fiber composite for efficient oxygen evolution reaction. *Catalysts* **2022**, *12*, 1242. [CrossRef]
26. Bai, L.; Lee, S.; Hu, X. Spectroscopic and electrokinetic evidence for a bifunctional mechanism of the oxygen evolution reaction. Angew. *Chem. Int. Ed. Engl.* **2021**, *60*, 3095–3103. [CrossRef] [PubMed]
27. Gao, Z.W.; Liu, J.Y.; Chen, X.M.; Zheng, X.L.; Mao, J.; Liu, H.; Ma, T.; Li, L.; Wang, W.C.; Du, X.W. Engineering NiO/NiFe LDH intersection to bypass scaling relationship for oxygen evolution reaction via dynamic tridimensional adsorption of intermediates. *Adv. Mater.* **2019**, *31*, e1804769. [CrossRef]
28. Dong, Q.; Wang, Q.; Dai, Z.; Qiu, H.; Dong, X. MOF-derived Zn-doped $CoSe_2$ as an efficient and stable free-standing catalyst for oxygen evolution reaction. *ACS Appl. Mater. Interfaces* **2016**, *8*, 26902–26907. [CrossRef]
29. Muráth, S.; Varga, T.; Kukovecz, Á.; Kónya, Z.; Sipos, P.; Pálinkó, I.; Varga, G. Morphological aspects determine the catalytic activity of porous hydrocalumites: The role of the sacrificial templates. *Mater. Today Chem.* **2022**, *23*, 100682. [CrossRef]
30. He, K.; Tadesse Tsega, T.; Liu, X.; Zai, J.; Li, X.H.; Liu, X.; Li, W.; Ali, N.; Qian, X. Utilizing the space-charge region of the FeNi-LDH/CoP p-n junction to promote performance in oxygen evolution electrocatalysis. *Angew. Chem. Int. Ed.* **2019**, *58*, 11903–11909. [CrossRef]
31. Yang, R.; Zhou, Y.; Xing, Y.; Li, D.; Jiang, D.; Chen, M.; Shi, W.; Yuan, S. Synergistic coupling of CoFe-LDH arrays with NiFe-LDH nanosheet for highly efficient overall water splitting in alkaline media. *Appl. Catal. B Environ.* **2019**, *253*, 131–139. [CrossRef]
32. Liu, J.; Wang, J.; Zhang, B.; Ruan, Y.; Lv, L.; Ji, X.; Xu, K.; Miao, L.; Jiang, J. Hierarchical $NiCo_2S_4$@NiFe LDH heterostructures supported on nickel foam for enhanced overall-water-splitting activity. *ACS Appl. Mater. Interfaces* **2017**, *9*, 15364–15372. [CrossRef]
33. Zhang, F.S.; Wang, J.W.; Luo, J.; Liu, R.R.; Zhang, Z.M.; He, C.T.; Lu, T.B. Extraction of nickel from NiFe-LDH into Ni_2P@NiFe hydroxide as a bifunctional electrocatalyst for efficient overall water splitting. *Chem. Sci.* **2018**, *9*, 1375–1384. [CrossRef]
34. Jia, B.; Xue, Z.; Liu, Q.; Liu, Q.; Liu, K.; Liu, M.; Chan, T.-S.; Li, Y.; Li, Z.; Su, C.-Y.; et al. Hierarchical nanotubes constructed from CoSe2 nanorods with an oxygen-rich surface for an efficient oxygen evolution reaction. *J. Mater. Chem. A* **2019**, *7*, 15073–15078. [CrossRef]
35. Kwak, I.H.; Im, H.S.; Jang, D.M.; Kim, Y.W.; Park, K.; Lim, Y.R.; Cha, E.H.; Park, J. $CoSe_2$ and $NiSe_2$ nanocrystals as superior bifunctional catalysts for electrochemical and photoelectrochemical water splitting. *ACS Appl. Mater. Interfaces* **2016**, *8*, 5327–5357. [CrossRef] [PubMed]
36. Zhao, S.; Jin, R.; Abroshan, H.; Zeng, C.; Zhang, H.; House, S.D.; Gottlieb, E.; Kim, H.J.; Yang, J.C.; Jin, R. Gold nanoclusters promote electrocatalytic water oxidation at the nanocluster/$CoSe_2$ interface. *J. Am. Chem. Soc.* **2017**, *139*, 1077–1080. [CrossRef]
37. Zan, G.; Wu, T.; Zhang, Z.; Li, J.; Zhou, J.; Zhu, F.; Chen, H.; Wen, M.; Yang, X.; Peng, X.; et al. Bioinspired nanocomposites with self-adaptive stress dispersion for super-foldable electrodes. *Adv. Sci.* **2022**, *9*, e2103714. [CrossRef] [PubMed]
38. Li, M.; Feng, L.G. $NiSe_2$-$CoSe_2$ with a hybrid nanorods and nanoparticles structure for efficient oxygen evolution reaction. *Chin. J. Struc. Chem.* **2022**, *41*, 2201019–2201024.
39. Zeng, X.; Zhang, H.; Zhang, X.; Zhang, Q.; Chen, Y.; Yu, R.; Moskovits, M. Coupling of ultrasmall and small Co P nanoparticles confined in porous SiO_2 matrix for a robust oxygen evolution reaction. *Nano Mater. Sci.* **2022**, *4*, 393–399. [CrossRef]
40. Xu, S.J.; Zhou, Y.N.; Shen, G.P.; Dong, B. $Ni(OH)_2$ derived from NiS_2 induced by reflux playing three roles for hydrogen/oxygen evolution reaction. *Chinese J. Struc. Chem.* **2022**, *41*, 2208052–2208057.
41. Wang, Z.; Zeng, S.; Liu, W.; Wang, X.; Li, Q.; Zhao, Z.; Geng, F. Coupling molecularly ultrathin sheets of NiFe-layered double hydroxide on $NiCo_2O_4$ nanowire arrays for highly efficient overall water-splitting activity. *ACS Appl. Mater. Interfaces* **2017**, *9*, 1488–1495. [CrossRef] [PubMed]
42. Song, F.; Hu, X. Exfoliation of layered double hydroxides for enhanced oxygen evolution catalysis. *Nat. Commun.* **2014**, *5*, 4477. [CrossRef] [PubMed]
43. Youn, D.H.; Park, Y.B.; Kim, J.Y.; Magesh, G.; Jang, Y.J.; Lee, J.S. One-pot synthesis of NiFe layered double hydroxide/reduced graphene oxide composite as an efficient electrocatalyst for electrochemical and photoelectrochemical water oxidation. *J. Power Sources* **2015**, *294*, 437–443. [CrossRef]
44. Yu, X.; Zhang, M.; Yuan, W.; Shi, G. A high-performance three-dimensional Ni–Fe layered double hydroxide/graphene electrode for water oxidation. *J. Mater. Chem. A* **2015**, *3*, 6921–6928. [CrossRef]
45. Zhong, H.; Liu, T.; Zhang, S.; Li, D.; Tang, P.; Alonso-Vante, N.; Feng, Y. Template-free synthesis of three-dimensional NiFe-LDH hollow microsphere with enhanced OER performance in alkaline media. *J. Electrochem. Soc.* **2019**, *33*, 130–137. [CrossRef]
46. Lin, Y.; Wang, H.; Peng, C.K.; Bu, L.; Chiang, C.L.; Tian, K.; Zhao, Y.; Zhao, J.; Lin, Y.G.; Lee, J.M.; et al. Co-induced electronic optimization of hierarchical NiFe LDH for oxygen evolution. *Small* **2020**, *16*, e2002426. [CrossRef]
47. Meng, L.; Xuan, H.; Wang, J.; Liang, X.; Li, Y.; Yang, J.; Han, P. Flower-like Co_3O_4@NiFe-LDH nanosheets enable high-performance bifunctionality towards both electrocatalytic HER and OER in alkaline solution. *J. Alloys Compd.* **2022**, *919*, 165877. [CrossRef]
48. Yang, Z.; Lin, Y.; Jiao, F.; Li, J.; Wang, J.; Gong, Y. In situ growth of 3D walnut-like nano-architecture Mo-Ni_2P@NiFe LDH/NF arrays for synergistically enhanced overall water splitting. *J. Energy Chem.* **2020**, *49*, 189–197. [CrossRef]

49. Zhang, Y.; Zhang, C.; Guo, Y.; Liu, D.; Yu, Y.; Zhang, B. Selenium vacancy-rich $CoSe_2$ ultrathin nanomeshes with abundant active sites for electrocatalytic oxygen evolution. *J. Mater. Chem. A* **2019**, *7*, 2536–2540. [CrossRef]
50. Liu, X.; Liu, Y.; Fan, L.-Z. MOF-derived $CoSe_2$ microspheres with hollow interiors as high-performance electrocatalysts for the enhanced oxygen evolution reaction. *J. Mater. Chem. A* **2017**, *5*, 15310–15314. [CrossRef]
51. Du, X.; Li, J.; Tong, K.; Zhang, X. Coupling $Co_2P/CoSe_2$ heterostructure nanoarrays for boosting overall water splitting. *Dalton Trans.* **2021**, *50*, 6650–6658. [CrossRef] [PubMed]
52. Liu, T.; Liu, Q.; Asiri, A.M.; Luo, Y.; Sun, X. An amorphous $CoSe_2$ film behaves as an active and stable full water-splitting electrocatalyst under strongly alkaline conditions. *Chem. Commun.* **2015**, *51*, 16683. [CrossRef] [PubMed]